J. Fluid Mech. (1997), *vol.* 350, *pp.* 119–147. Printed in the United Kingdom

© 1997 Cambridge University Press

Ringing of a vertical cylinder in waves

By J. R. CHAPLIN[1], R. C. T. RAINEY[2,3] AND R. W. YEMM[1]

[1] Department of Civil Engineering, City University, London EC1V 0HB, UK

[2] Centre for Non-linear Dynamics, University College London, Gower Street, London WC1E 6BT, UK

[3] WS Atkins Consultants Ltd, Ashley Road, Epsom, Surrey KT18 5BW, UK

(Received 10 April 1996 and in revised form 16 May 1997)

This paper analyses the results of two series of experiments concerned with the response of a single vertical cylinder in the inertia regime in steep non-breaking waves. We recorded first the loading on a cylinder when it was held stationary, and secondly, its response in the same waves when it was pivoted just above the floor of the wave flume, and supported at the top by springs in the horizontal plane. Spring stiffnesses were set to achieve natural frequencies (measured in still water) in the range between 3 and 11 times the dominant wave frequency. The experiments were repeated with cylinders of three different diameters.

Peak loading on stationary cylinders was found to exceed the predictions of a Morison model (based on kinematics computed from a numerical model of the measured waves), though improvements were achieved through the inclusion of slender-body terms. Measured ringing responses are generally in good agreement with those computed on a quasi-static basis from the measured loading history, but in some conditions, particularly at low frequency ratios, there is clearly some feedback from the motion to the excitation. Peak accelerations in the steepest waves are found to be limited approximately to those that would occur if the maximum loading were applied as a step change. Particular attention is given to a rapid cycle of loading that occurs after the crest has passed the cylinder's axis, and to images of the flow around the cylinder at the water surface.

1. Introduction

The natural frequencies of offshore structures are generally well above the frequency corresponding to the peak of the wave spectrum. Conventional frequency domain approaches are capable of predicting the linear part of the resonant response, and second-order diffraction programs can in principle predict the sum-frequency excitation that gives rose to 'springing'. Evidence in extreme waves of 'ringing', a potentially more dangerous nonlinear motion with burst-like characteristics, was found in model tests of deep-water oil production platforms for the Heidrun, Draugen and Troll fields in the Norwegian Sea (Natvig & Teigen 1993). Unlike springing, ringing has a severely non-Gaussian nature, generates very high stress levels within a burst of only a few oscillations, and occurs only during the passage of very steep waves. Theoretical and numerical predictions of ringing are subject to significant uncertainties because an adequate understanding of the underlying physical processes has not been reached.

Besides the kinematics of steep waves that generate ringing, parameters that are probably important are the shape of the columns at the water surface, interaction between neighbouring columns, and the height of the centre of gravity of the structure.

https://doi.org/10.1017/S002211209700699X Published online by Cambridge University Press

Most of the previous experimental work on ringing has been carried out with the purpose of investigating cases of some geometrical complexity, but there is also much to be said for studying the problem of a single surface-piercing vertical cylinder in steep waves. This paper describes laboratory experiments on ringing in this very simple configuration, undertaken with the aim of furthering an understanding of the process, and, through the provision of well-documented data, of contributing to the validation of existing methods of analysis.

The problem of predicting ringing responses has stimulated experimental and theoretical work on the flow around fixed vertical cylinders in steep waves (e.g. Grue, Bjørshol & Strand 1993; Stansberg *et al.* 1995; Faltinsen, Newman & Vinje 1995; Malenica & Molin 1995), in the expectation that once the loading is known, the motion may be computed by routine techniques. In experimental work by Grue *et al.* large waves were generated, as in the present case, by frequency focusing. In Stansberg *et al.* individual extreme events were identified by inspection from within a long sequence of irregular waves. Though in some respects this may be more realistic, frequency focusing offers much better control over the location and timing of a large wave, and over its amplitude. Theoretical work by Faltinsen *et al.* and Malenica & Molin follows a perturbation approach in which the frequency content of the loading is restricted to the first few harmonics of the wave frequency. In slender-body theory on the other hand (Rainey 1995*a*, *b*) fully nonlinear terms are derived for the limiting case of bodies whose waterplane dimensions are small in comparison with all other scales of the problem.

In the work described below we compare measurements of the cylinder's response with that obtained by integration of its equation of motion, using as excitation the loading measured on it when stiffly supported in the same waves. On the whole agreement is good, though particularly at low frequency ratios it is clear that the cylinder's motion does influence the loading. We first present records of the forces on a stationary cylinder in the inertia regime in steep focused waves and compare the results with those of Morison's equation and slender-body theory, using the kinematics computed from a numerical model of the measured waves, and from nonlinear regular waves of similar height and period. Measurements of response at frequency ratios between 3 and 10 show that an important factor is the time scale of a rapid reversal of loading under the crest. When this matches the period of the cylinder's natural frequency oscillations it leads to a substantial cancellation of the motion after the first cycle. Conversely when the time interval between positive and negative peak forces coincides roughly with 50 % or 150 % of the cylinder's period, the motion is enhanced.

2. Experimental arrangement

2.1. *The wave environment*

Measurements of loading and response were carried out in a wave flume that is 18 m long and 750 mm wide, with a mean water depth of 525 mm. The flume is equipped with an absorbing bottom-hinged waveboard, and at the other end with a wave energy dissipater comprising a vertical wedge of firm poly-ether foam whose apex points towards the waveboard at a distance of 15.4 m. Wave reflections, measured by slowly towing a wave gauge through regular waves, were less than 3 % when expressed as a ratio of wave heights.

For purposes of harmonic analysis it might be thought desirable to study ringing in regular waves. The difficulty with this however is that at realistic levels of damping the cylinder's response would last much longer than the wave period. For example, the

https://doi.org/10.1017/S002211209700699X Published online by Cambridge University Press

Wave	745	750	755	760	765	770	775
$2A$ (m)	0.115	0.128	0.143	0.158	0.172	0.186	0.205
k (m^{-1})	3.63	3.60	3.56	3.52	3.48	3.43	3.37
kA	0.208	0.230	0.255	0.278	0.299	0.319	0.345
η_{max} (m)	0.073	0.082	0.093	0.104	0.114	0.124	0.138
$(\partial\eta/\partial t)_{max}$ (m s^{-1})	0.37	0.43	0.51	0.61	0.73	0.92	1.26
Time of $(\partial\eta/\partial t)_{max}$ (s)	−0.17	−0.15	−0.14	−0.10	−0.10	−0.07	−0.05
$(\partial\eta/\partial t)_{min}$ (m/s)	−0.37	−0.42	−0.47	−0.51	−0.54	−0.56	−0.55
Time of $(\partial\eta/\partial t)_{min}$ (s)	0.18	0.16	0.12	0.10	0.10	0.10	0.11

TABLE 1. Characteristics of waves at the focus point. In all cases the still water depth was 0.525 m and the period between troughs was close to 1.05 s.

present experiments were carried out in a tank where regular waves would have had periods of around 1 s. In the measurements of response shown below, the cylinder's amplitude of motion 1 s after the initial excitation was typically well over 50 % of its maximum, and oscillations were still noticeable 10 s later. In regular waves therefore the cylinder's response to each burst of excitation would be very much influenced by its existing decaying oscillations. While a periodic motion might develop, this would probably be more difficult to understand than the response to an isolated event, and it would not be representative of conditions offshore where the large waves that are likely to generate ringing appear singly rather than as members of a regular train (Atkins, Lyons & Rainey 1997).

Some measurements of the loading on stiffly supported cylinders were, however, attempted in regular waves. But the useful range of conditions was restricted by the fact that when the incident waves were greater than about 65 % of their limiting height, reflections that propagated from the cylinder in the opposite direction generated some local breaking of the surface. Force measurements were made with the 100 mm diameter cylinder in waves of heights below this limit and the fundamental frequency component was found in each case to be in excellent agreement with a Morison equation prediction based on stream-function wave theory (see below). But the waves were not steep enough for the higher frequency components of the loading to be of a sufficient magnitude to warrant further study.

We carried out all other experiments in single large waves, generated as described below and in the Appendix. The waves were focused at a point 12.5 m from the waveboard by appropriate modulation, in frequency and amplitude, of the waveboard's control signal. This consisted of a summation of 34 continuous sinusoidal components whose frequencies were equally spaced between 0.511 and 1.244 Hz. For each wave condition the control signal was generated by an iterative technique, based on the requirement that as far as possible all wave components should come to the same phase (corresponding to maximum horizontal particle velocity) at the focus point. Further details are given in an Appendix, and in Chaplin (1996). Measurements around the focus point showed that components of the focused wave were more cohesive than indicated by the linear dispersion relationship (see figure 22 in the Appendix), and that the maximum crest elevation (and the point where wave breaking occurred if the waves were of sufficient amplitude) was about 1 m further along the flume away from the waveboard.

Heights, steepnesses, and other features of the seven focused waves used in the present experiments are set out in table 1, where the wave height $2A$ is the difference between the elevations of the crest and the preceding trough. Records of water surface

https://doi.org/10.1017/S002211209700699X Published online by Cambridge University Press

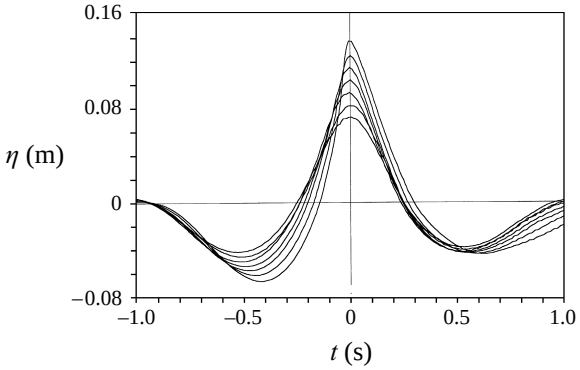


FIGURE 1. Water surface elevation records of the seven focused waves used in the experiments.

elevations $\eta(t)$ at the focus point, obtained in the absence of the cylinder, are shown in figure 1, where, as elsewhere in this paper, time t is set to zero at the instant when the wave crest passed the cylinder's axis. All features of the experiments displayed a very high degree of repeatability. Efficient absorption of waves at both ends of the flume ensured that the motion of the water decayed very rapidly indeed after each test.

Table 1 also shows a representative wavenumber k for each case, determined from the height $2A$, and a wave period of 1.05 s, being close to the observed interval between the troughs before and after the focused wave in all cases. In view of the observed cohesiveness of the wave crest just described, the wavenumber was obtained from a stream-function solution for a *regular* wave, of the same height and period, in the same still water depth.

The 16th-order steam-function code used for this purpose and subsequently for some of the computations of particle velocities follows the approach described by Chaplin (1980), and was checked against Cokelet's (1977) tabulated data for conditions close to those of the experiments, where kh was about 2.0 (h being the still water depth). Crest elevations and particle velocities at the crest were found to be in agreement to within 0.2%, for wave steepnesses up to 3% of limiting height.

For reference purposes table 1 gives peak rates of change of the water surface elevation $\partial\eta/\partial t$ measured in the experiments at the cylinder's location. In the smallest waves, those before and after the crest are of almost equal magnitudes, and the times at which they occur are almost symmetrically disposed about $t = 0$. And in accordance with the behaviour of regular waves of large amplitude, where the points of maximum surface slope converge towards the crest (and in limiting conditions coincide at the 120° corner), these times approach $t = 0$ as the wave amplitude is increased. But the largest waves were asymmetrical, having a rise time on the front face considerably shorter than the fall time on the rear face; see figure 1.

All of the force and response measurements were made in the 750 mm wide wave flume described above. However, flow visualizations were carried out in a second series of tests in a wave flume that is 12 m long, 400 mm wide, and has a still water depth of 700 mm. This is equipped with a waveboard and wave absorber similar to those in the 750 mm wide flume, and control signals were computed (over the same range of frequencies as before) to achieve focused waves 8.5 m from the waveboard (rather than the 12.5 m in the original flume). The 400 mm wide flume provided better access for visualization of the free surface, and images were obtained by direct capture to RAM of the output of a CCD camera at a rate of 50 frames per second. The free surface was lit by floodlights directed upwards through the glass floor of the flume. To ensure

https://doi.org/10.1017/S002211209700699X Published online by Cambridge University Press

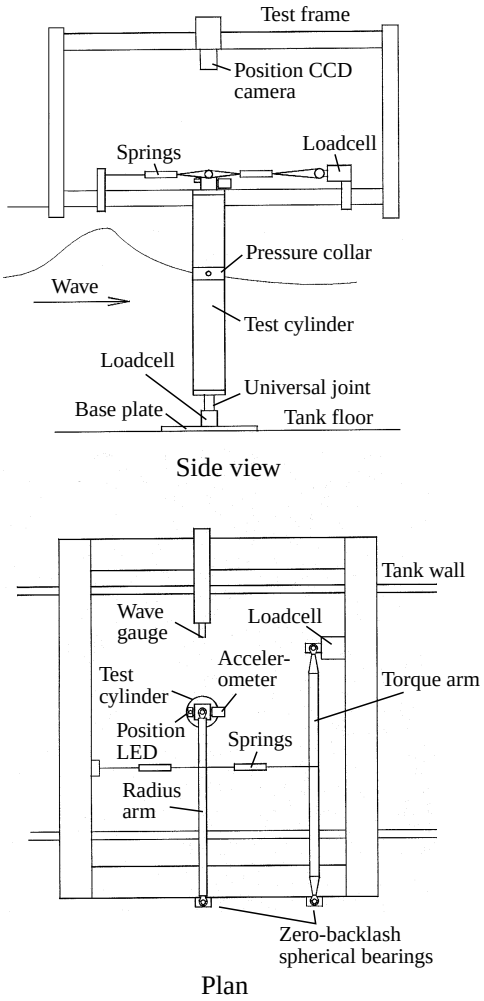


FIGURE 2. Layout of the experimental arrangments.

accurate time registration, acquisition of the images was triggered from the command signal played out to the waveboard.

2.2. *The test cylinders*

Measurements of loading and response were made with cylinders of outside diameters 100 mm and 127 mm, constructed from Perspex pipe of 3 mm wall thickness. The cylinders were empty, so that their total inertia (dominated by the effects of added mass) should be representative of that of a steel or concrete tube. A third similarly constructed cylinder of 70 mm diameter was also used in the tests, but not all of the results from this cylinder are reported here since they were quite strongly affected by drag. The arrangements for mounting the cylinders at the focus point in the 750 mm wide flume are shown in figure 2; each cylinder was pivoted at the bottom (100 mm above the flume floor) and supported at the top on springs in the horizontal plane, with a lever mechanism that provided for an easy and continuous adjustment of stiffness. It was found that ringing did not induce significant lateral response, and so the support system was designed to allow motion only in the longitudinal direction. Experiments

https://doi.org/10.1017/S002211209700699X Published online by Cambridge University Press

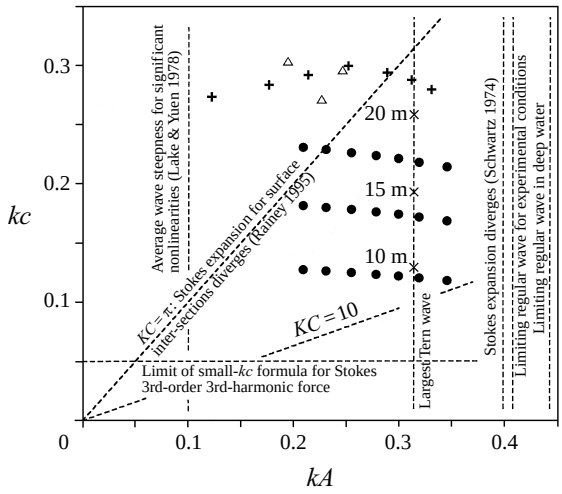


FIGURE 3. Experimental and other conditions on the (kA, kc)-plane. Present experiments (●); Grue *et al.* (1993) (+); Stansberg *et al.* (1995) (△). Wavenumbers for the experimental data were obtained from nonlinear regular wave theory using the measured trough-to-trough period. Points marked × represent the conditions corresponding to members of 10 m, 15 m and 20 m diameter in the largest wave observed at the Tern Platform (Atkins *et al.* 1997). Limiting wave amplitudes are calculated from Cokelet (1977); that for the experimental conditions refers to the actual mean water depth and the measured trough-to-trough period.

were carried out with stiffnesses set to achieve natural frequencies (measured in still water) within the range 2.87 to 11.27 Hz. The structural damping factor of the cylinders (measured in free vibration tests in air) was about 0.5%.

The cylinders were mounted at top and bottom on load cells, while the 100 mm cylinder was also fitted with a ring of 12 flush-mounted pressure transducers at an elevation 10 mm below still water level. The motion at the top of each cylinder was recorded both with an accelerometer, and with a non-intrusive optical displacement meter. All channels of data (totalling five for the 70 mm and 127 mm cylinders, and 17 for the 100 mm cylinder) were sampled at 182.04 Hz.

All of the flow visualization experiments were carried out with the 100 mm diameter cylinder in the 400 mm wide flume (at the same blockage ratio as that of Grue *et al.* 1993). We first investigated the effects of channel blockage in the 750 mm flume, by installing sidewalls that reduced its width to 400 mm. Force records obtained in similar waves with and without sidewalls were almost indistinguishable, except that when the flume width was reduced, there was a slight increase in the peak force. In the largest wave (775) this amounted to 8%; in wave 760, it was no more than 2.5%. These results support the view that none of the present measurements are significantly contaminated by blockage effects. Quite different limitations apply in regular waves. For example, theoretical and experimental data given by Zhao *et al.* (1988) for the case of a sphere of 1 m diameter in a tank 10.5 m wide and 10 m deep indicate that tank wall effects are very much more important than those found here. In the present case the motion is highly transient, and it seems likely that there is not sufficient time for substantial transverse reflections to develop within the period of interest.

Forces at the top of the cylinder were measured also in the visualization tests, in order to ensure that images were captured at the times of specific events in the loading history.

https://doi.org/10.1017/S002211209700699X Published online by Cambridge University Press

2.3. *Theoretical considerations*

The wavenumbers of table 1, and the cylinder diameters just described, give kc values (where c is the cylinder radius) of around 0.12, 0.18 and 0.22. Also, the wave amplitudes A put the nominal surface Keulegan–Carpenter number KC (defined as $\pi A/c$) in the range 3–10. The three cylinders are therefore in the 'inertia', rather than the 'drag' or 'diffraction', regime. To compare this experiment with others, it is convenient to consider a (kA, kc) plane, as in figure 3, on which we can locate the present experimental conditions, and those of Grue *et al.* (1993) and Stansberg *et al.* (1995). This plane can also be used to illustrate the various theoretical considerations which bear on the experiment, as we now describe.

First, the vertical lines show the limits of various wave theories. On the left, we show the lower limit kA identified by Lake & Yuen (1978) as the average wave steepness of a group in which significant nonlinear effects on phase speeds are to be expected. This is to emphasize the fact that the focused waves in the experiments are all likely to exhibit the strongly nonlinear dispersion mentioned earlier (see figure 22 in the Appendix). Then, we show the limiting steepness of the regular waves which we have accordingly sometimes used to model them, as described in the discussion of table 1. The steepest waves used in the experiments evidently had about 85% of the maximum height of regular waves of the same period and water depth. For completeness, we also show the maximum steepness in deep water, and, at $kA = 0.40$, the steepness near which the Stokes expansion for undisturbed waves diverges (Schwartz 1974). Finally, to emphasize the relevance of the experiment to full-scale structures, we show a vertical line corresponding to the largest wave recorded during the 1990–92 measurements at the Tern platform in the North Sea (Atkins *et al.* 1997 – nonlinear regular wave theory is used to compute the steepness, which is here $kA = 0.314$, based on the measured height of 26.92 m and upcrossing period of 12.50 s). We also show the points on this line which correspond to this wave combined with structural members of diameters 10 m, 15 m and 20 m.

Next, diagonal lines correspond to different values of the nominal surface Keulegan–Carpenter number $\pi A/c$. We show the line $KC = 10$; all points below this line have higher KC, and are thus increasingly dominated by drag forces. It may be seen that the smallest of the three cylinders is close to this line in the largest waves, and thus that drag forces were beginning to be important there, as noted earlier. We also show the line $KC = \pi$ (i.e. wave height = cylinder diameter). According to Rainey (1995*b*) the Stokes expansion (in which the boundary conditions of ascending order are applied at the still-water position) can be expected to diverge for all points below this line, because of the presence of the cylinder. This is an important theoretical point. Rainey's argument is based on the solution of a much simpler problem in which the water surface is constrained by a 'wavy lid', so as to keep the shape it would have were the cylinder absent. Applying the Stokes expansion is here analogous to using it to solve the simple two-dimensional problem of flow around a fully immersed cylinder oscillating in still water by applying successive boundary conditions at the mean cylinder position, rather than at its instantaneous displaced position. This scheme can easily be shown to diverge once the peak-to-peak cylinder excursions exceed the cylinder diameter (Rainey 1995*b*).

Finally, horizontal lines in figure 3 correspond to particular features of Stokes expansion solutions. The simplest would be the threshold of Stokes first-order diffraction effects, which, at $kc \approx 0.5$, is a line above the top of the figure, placing the whole experiment in the 'inertia regime' as already noted. An exactly analogous line

https://doi.org/10.1017/S002211209700699X Published online by Cambridge University Press

is the threshold of Stokes third-order diffraction effects, i.e. the value of kc above which there are significant errors in the small-kc asymptotic form (namely a third-harmonic component of amplitude $2(\rho g\pi c^2/k)(kA)^3$) of the Stokes third-order diffraction force. This has recently been established by Malenica & Molin (1995) as $kc = 0.05$. For points above this line, diffraction is important in this sense. Evidently it would be important for all the present experimental cases had the divergence of Stokes's expansion not made the point irrelevant. The original claims for this asymptotic form were based on its derivation by an alternative perturbation scheme (Faltinsen, Newman & Vinje 1995), that was claimed to be valid for the region of the present experiments. The free-surface observations below, however, which feature local breaking of the water surface near the cylinder, show that we do not have smooth flow conditions – therefore *all* perturbation schemes (and not merely the Stokes expansion) must break down.

As far as these violent motions of the free surface are concerned, there appears to be a fruitful analogy with a cylinder moving from rest in still water, at constant velocity (Rainey 1997). Here there is a step change in the cylinder's acceleration relative to the water, just as there is when a sharp (120°) crested wave passes a fixed cylinder. And a small-time expansion shows, very simply, that there should again be violent motions of the free surface.

3. Experimental results

3.1. *Peak loading on a stiffly supported cylinder – comparison with computations*

To measure the loading on a stiffly supported cylinder, the top springs shown in figure 2 were replaced by stiff links, producing natural frequencies of about 28 Hz for all three cylinders and making the dynamic 'ringing' response very small. The moments $M(t)$ about the tank floor obtained in this way, on each of the three cylinders, in each of the seven focused waves, are plotted in figure 4. These unfiltered results have maxima and minima in each case near to points identified as M_1, M_2, M_3 and M_4, which represent the corresponding extreme values after numerical filtering had removed the effects of dynamic response. In each case the peak moment M_1 occurred at about the same time as the maximum in $\partial\eta/\partial t$.

For the purpose of obtaining numerical predictions of the loading, it was necessary to model the undisturbed flow beneath the waves. One approach to this problem would be to match the water surface elevation records to a time-stepping code for time-dependent waves (e.g. New, McIver & Peregrine 1985; Dommermuth *et al.* 1988), but this would be a major undertaking. Instead we used the simpler crest-fitting technique described by Baldock & Swan (1994) in which a section of a single measured water surface elevation record (in our case 3.3 s centred at the instant when the crest passed the cylinder's position) is assumed to be periodic in both time and space. The flow is represented by a velocity potential composed of a number of frequency components (in our case, the first 20 multiples of the fundamental $2\pi/3.3\ \mathrm{s}^{-1}$), at each of which there are as many wavenumbers (the first 20 multiples of $2\pi/7.25\ \mathrm{m}^{-1}$). The 400 complex coefficients of the velocity potential series are computed by a least-squares method that aims to minimize differences between the measured and predicted water surface elevation record, and errors in the free-surface boundary conditions over the entire domain of the simulation. The technique adopted here followed closely that described by Baldock & Swan, except that the dynamic boundary condition was satisfied implicitly at each iteration (as in Chaplin 1996).

This method was tested in conditions similar to those of the present experiments by Baldock, Swan & Taylor (1995), who showed that it gave particle velocities in close

https://doi.org/10.1017/S002211209700699X Published online by Cambridge University Press

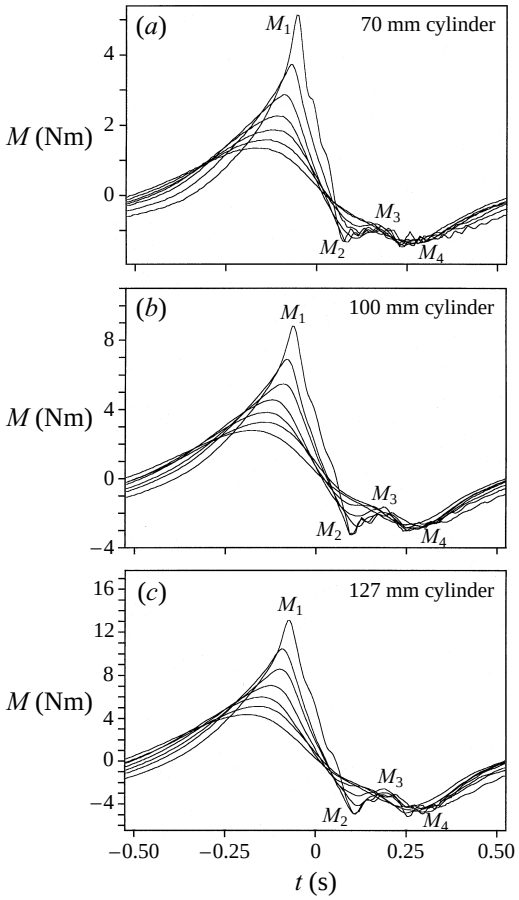


FIGURE 4. Moments recorded on the three cylinders when stiffly supported in each of the focused waves of table 1. These records are unfiltered, and the moment axes are scaled in each case in proportion to the square of the cylinder's diameter.

agreement with measurements made by laser Doppler anemometry. Also, Chaplin (1996) found that it correctly modelled the behaviour of the crest for some distance on either side of the focus point. These earlier validations provided confidence in the method, and we used it to compute the kinematics of waves up to case 765. The solutions for cases 770 and 775 failed to converge. It seems reasonable to link this with the fact that in the laboratory, these waves (and not the smaller ones) broke further along the tank.

In figure 5 the numerical solution for case 765 is plotted in the form of (*a*) time histories of water surface elevations at seven points around the focus, and (*b*) water surface profiles at seven different times. The simulation matches the measurements at the focus $x = 0$ m, and it is seen that (as observed in the laboratory and mentioned above) the computed elevation of the crest achieves a maximum after passing this point. In the simulations, the dynamic boundary condition at the free surface was satisfied exactly; the root-mean-square error in the kinematic boundary condition, expressed as a proportion of the root-mean-square surface particle velocity, was 6.4% for case 745, rising to 7.3% for case 765.

A second method for computing wave kinematics was to use a regular-wave model

https://doi.org/10.1017/S002211209700699X Published online by Cambridge University Press

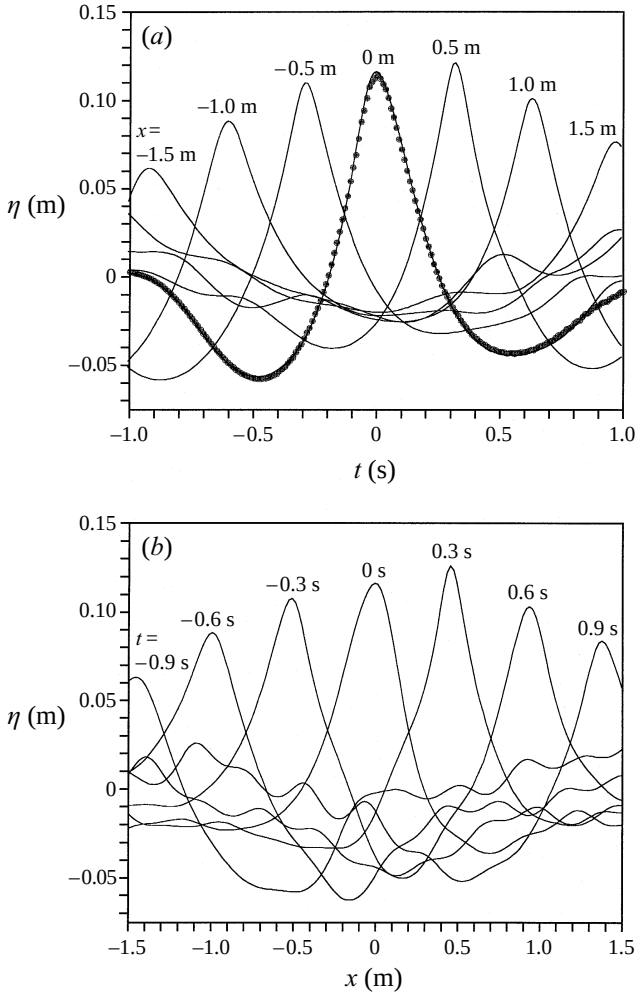


FIGURE 5. Computed water surface elevations for case 765, (*a*) as functions of time at seven different locations (the measurements at the focus point $x = 0$ m are shown as points), and (*b*) as functions of x at seven different times.

on the basis that this represents a simply defined and widely accessible standard solution, capturing many of the nonlinear features of the focused waves, and in particular their cohesiveness, as discussed earlier. The use of regular-wave models also, of course, follows conventional design practice for offshore structures. For these reasons some comparisons are made below between force measurements and predictions based on stream function solutions for regular waves described above.

For case 765, figure 6 shows the results of various computations of the loading on the 100 mm cylinder, based on each of these methods, as well as the corresponding measurements. For the two larger cylinders, figure 7 shows maximum measured and computed positive moments in the dimensionless form $M_1' = M_1 k/(\rho g \pi c^2 h)$.

The first load computations are based on the Morison inertia term alone, with an inertia coefficient of two. This calculation used the total acceleration (including the convective contribution) in the incident wave, and integrated the inertia force up to the instantaneous undisturbed water surface. The Morison drag (applied in the same way

https://doi.org/10.1017/S002211209700699X Published online by Cambridge University Press

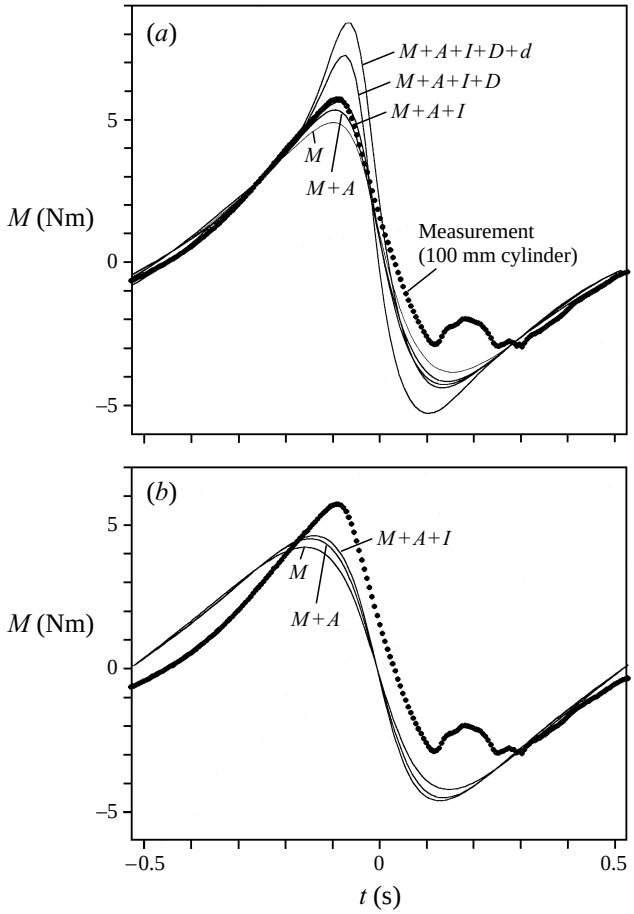


FIGURE 6. Moment records for the 100 mm cylinder in case 765 compared with predictions based on (*a*) unsteady and (*b*) regular wave kinematics. Force components are identified in figure 7.

and based on a drag coefficient of 1.0) is also shown in figures 6 and 7 after the addition of further potential flow forces.

These cover the refinements to the Morison inertia term described in Rainey (1995*b*), which bring its accuracy, when applied in this way, up to second order in the Stokes expansion, for the case of a slender cylinder (i.e. small kc). For the present simple fixed geometry these are first, the 'axial divergence force', which is integrated like the Morison inertia term:

$$\int_{-h}^{\eta} \rho\pi c^2(\partial v_z/\partial z)\, v_x \,\mathrm{d}z, \tag{1}$$

where v_x and v_z are the horizontal and vertical particle velocity components, the former measured in the same sense as the force, and z measured upwards from the still water level. Secondly, there is the 'surface intersection force', which is applied as a point load:

$$-(\rho\pi c^2/2)\, v_x^2\, \partial\eta/\partial x, \tag{2}$$

at the instantaneous intersection point of the cylinder axis with the incident wave surface.

https://doi.org/10.1017/S002211209700699X Published online by Cambridge University Press

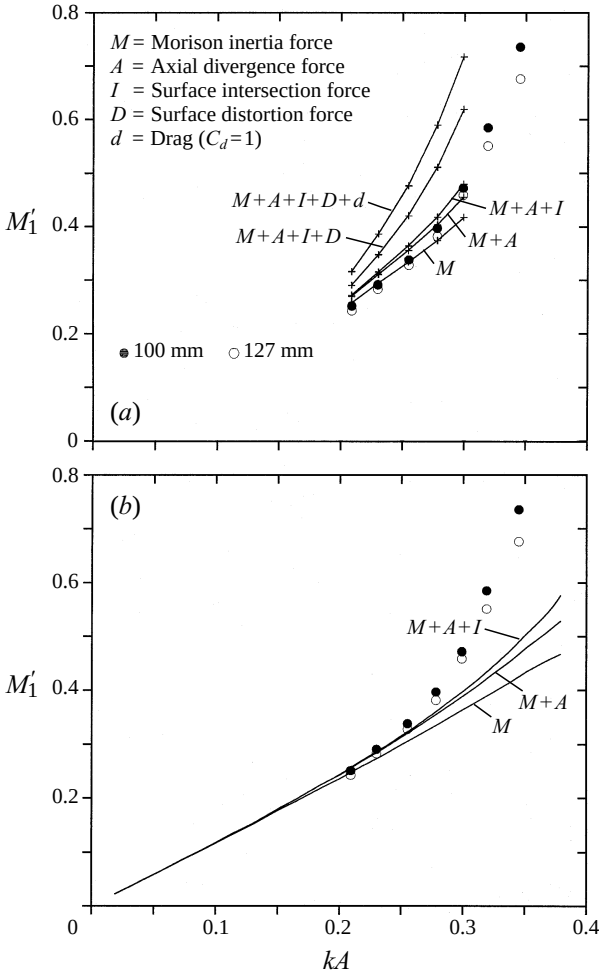


FIGURE 7. Peak normalized moments as a function of wave steepness. Measurements from the 100 mm and 127 mm cylinders are compared with Morison and slender-body forces computed from (*a*) unsteady and (*b*) regular wave kinematics.

There remains a third-order error when compared with the Stokes asymptotic form $2(\rho g\pi c^2/k)(kA)^3$ mentioned above. This can be removed by an additional 'surface distortion force':

$$(7\rho\pi c^2/2g)\, v_x^2\, \partial v_x/\partial t, \tag{3}$$

which is again applied as a point load at the surface intersection. However, in contrast to the 'surface intersection force' (2), whose derivation rests on elementary considerations of energy conservation (Rainey 1995*b*, figure 1), the derivation of (3) (described in Rainey 1995*a*) assumes the smooth-flow conditions of small surface distortion compared with the cylinder diameter (i.e. the Stokes assumption of small kA). This is plainly inappropriate in the present experiments, and the comparison with the Stokes expansion is anyway irrelevant, because it has diverged, as discussed in the previous section.

Figures 6(*a*) and 7(*a*) suggest that good agreement with the positive measured moment is obtained when just the first two slender-body terms (1) and (2) are included.

https://doi.org/10.1017/S002211209700699X Published online by Cambridge University Press

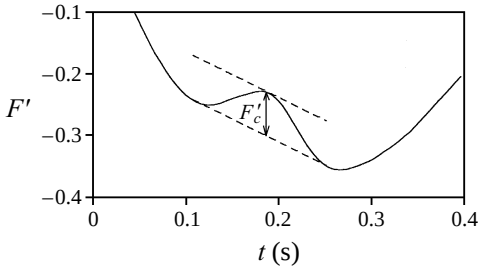


FIGURE 8. Definition sketch for F_c', a measure of the magnitude of the secondary loading cycle. The force record shown is for the 100 mm cylinder in case 760.

This supports the view that the 'surface distortion force' (3) should be dispensed with, since it is difficult to justify theoretically in these conditions, as explained above. Equally, the computed drag appears inappropriate, probably because of the highly unsteady nature of the flow.

From figures 6(*b*) and 7(*b*) it is seen that the regular wave model is in rather poor agreement with the measurements, and the sum of Morison, axial divergence and surface intersection forces results in a significant under-prediction of the peak loading. Agreement is better when the surface distortion and drag forces are included, but since this is only fortuitous, these components are omitted. Clearly the kinematics of the focused wave are more severe than those of a regular wave of equivalent height and period.

3.2. *Secondary loading cycle*

It is worth considering in more detail the loading that was observed after the crest had passed the cylinder's axis, when there were large discrepancies between the measurements and predictions, as shown in figure 6. In steep waves the moment fell to the minimum identified as M_2 in figure 4, followed by a rise to M_3 and a fall to another minimum at M_4. In case 745 the minimum in $\partial\eta/\partial t$ coincided with M_4; in case 775 it coincided with M_3. The moment M_2 became more negative as the wave steepness was increased, but in dimensionless terms M_4 was remarkably constant for all waves and both the larger cylinders, with $M_4' = -0.341 \pm 6\%$. The 'secondary loading cycle' M_2, M_3, M_4 is shown below to have a significant effect on the response of a cylinder mounted on more flexible supports. This cycle was observed also by Grue *et al.* (1993) and can be seen in the force records of Stansberg *et al.* (1995). Grue *et al.* noted that it lasted for about 15% of the wave period (defined as the local zero up-crossing period at the position of the cylinder's axis), had a magnitude of up to 11% of the peak-to-peak range of the total force, first occurred when the Froude number

$$Fr = \eta_{max}\omega/(2gc)^{1/2} \tag{4}$$

exceeded about 0.35, and became pronounced when $Fr > 0.4$. They attributed it to a suction force acting at about one cylinder radius below the still-water level. Our measurements of the duration of the secondary loading cycle (about 0.15 s for all three cylinder diameters) and its magnitude (up to between 8% of the total force for the smallest cylinder, and 12% for the largest) are in agreement with those of Grue *et al.* However, in the present case, it could not be considered to be 'pronounced' until the Froude number exceeded about 0.6, and then not in all cases. Nor was its appearance dependent solely on the Froude number.

A measure of the magnitude of the secondary loading cycle F_c' is defined in figure 8 in terms of the total horizontal force on the cylinder $F(t)$ normalized with respect to

https://doi.org/10.1017/S002211209700699X Published online by Cambridge University Press

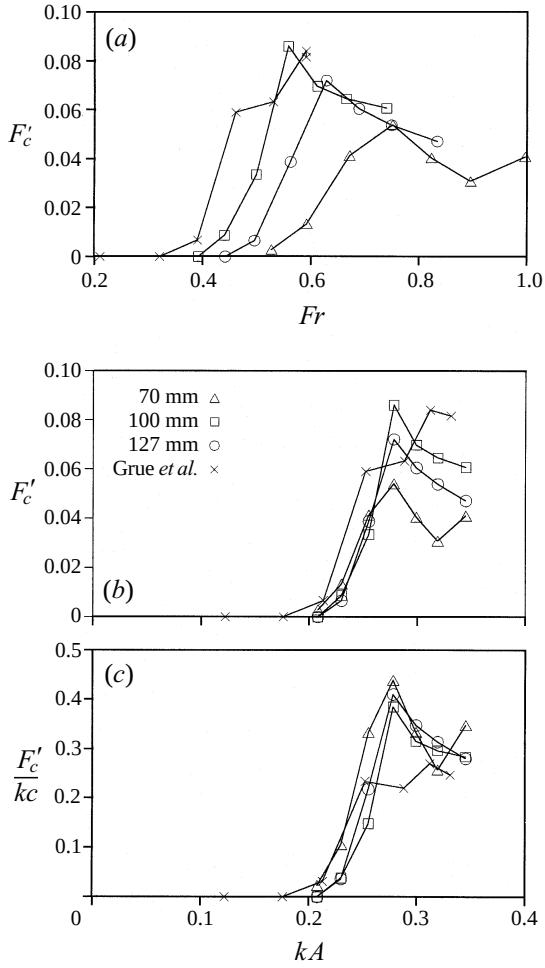


FIGURE 9. The normalized magnitude of the secondary loading cycle, plotted (*a*) against the Froude number (equation (4)), (*b*) against wave steepness, and (*c*) after division by kc, against wave steepness.

$\rho g\pi c^2/k$. A slightly different definition was adopted by Grue *et al.*, whose data are however re-analysed here in the same way as our own. Figure 9(*a*) shows that values of F_c' from the four sets of data are not well correlated when plotted against the Froude number Fr defined above. Froude numbers from the data of Grue *et al.* have also been re-calculated for present purposes using a frequency ω in equation (4) corresponding to the trough-to-trough period, and not (as in Grue *et al.*) the central frequency of the wave packet. But figure 9(*a*), and the similarity of the moment records from all three cylinders (figure 4), make it clear that the amplitude of the secondary loading cycle is not solely dependent on the Froude number, however its velocity scale is defined. With respect to the initial growth of the process, much better agreement appears when the same data are plotted against kA, as in figure 9(*b*), suggesting that in this connection the Froude number is less important than the wave steepness.

In the largest waves, the values of F_c' derived from the present measurements decrease with increasing wave steepness but are roughly proportional to the cylinder's diameter, as is shown in figure 9(*c*) where F_c'/kc is plotted against kA. This behaviour suggests a relationship between c^3 and the magnitude of the secondary loading cycle in

https://doi.org/10.1017/S002211209700699X Published online by Cambridge University Press

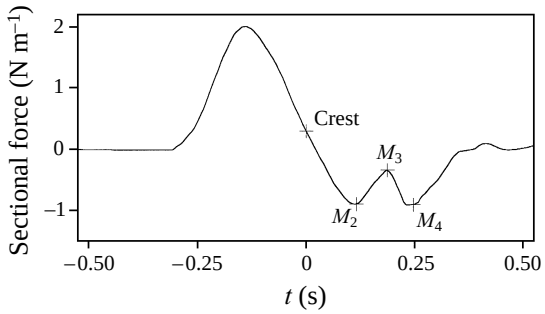


FIGURE 10. Sectional force record integrated from pressure measurements on the 100 mm cylinder in case 765. Pressure distributions at times corresponding to the crest, M_2, M_3 and M_4 are shown in figure 11.

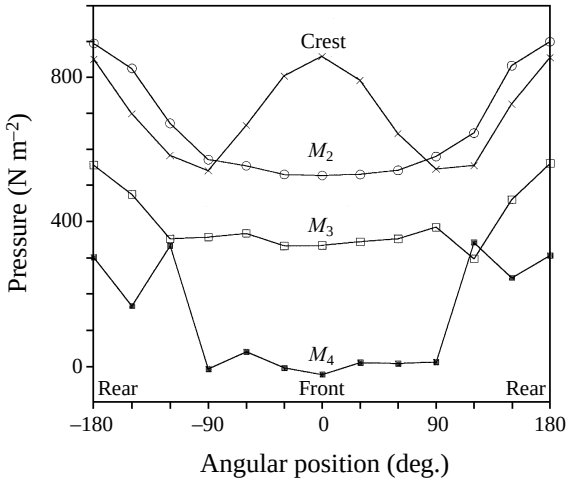


FIGURE 11. Pressure distributions around the 100 mm cylinder in case 765 at times corresponding to the crest, and to M_2, M_3 and M_4.

the largest waves, possibly through the appearance of a wave whose length is related to the cylinder's diameter.

The same cycle of loading may be seen in the pressure measurements. The sectional force record integrated from pressure distributions 10 mm below still-water level for the 100 mm cylinder in wave 765, plotted in figure 10, shows a pronounced oscillation over a range equal to one-quarter of the peak force per unit length. Distributions of pressure around the cylinder at four instants (identified in figure 10) corresponding to the crest, and to the extremes M_2, M_3 and M_4 of the oscillation for wave 765 are shown in figure 11. The increase in loading M_2 to M_3 is clearly associated with the fact that over this interval the pressure falls more rapidly on the rear face of the cylinder than on the front, while the reverse is true between M_3 and M_4.

3.3. *Observations of the free surface*

At the time corresponding to M_1, coinciding almost with the maximum horizontal fluid acceleration in the wave (i.e. the maximum wave slope), the water surface is raised on the up-wave side of the cylinder and lowered on the down-wave side. As expected this

https://doi.org/10.1017/S002211209700699X Published online by Cambridge University Press

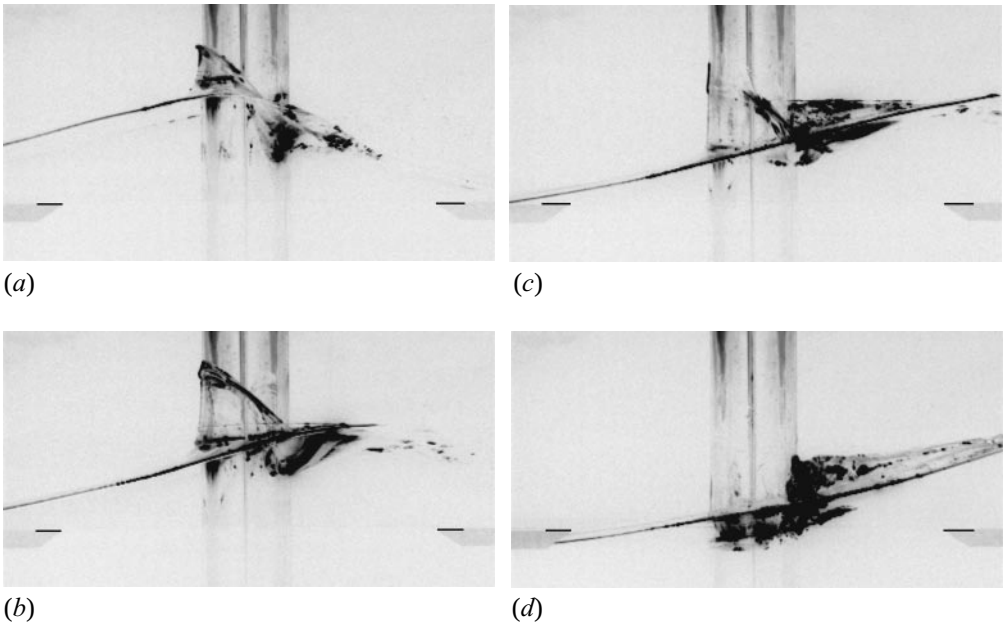


FIGURE 12. Flow around the 100 mm cylinder in case 765. Horizontal lines at the edge of each frame are at still water level. The times are (*a*) when the crest is alongside the cylinder, (*b*) at M_2, (*c*) at M_3 and (*d*) at M_4.

follows the Stokes first-order water pressure distribution (i.e. that responsible for the Morison inertia force, which is at a maximum at this stage). Observations of the free surface around the cylinder at four later times are reproduced as negative images (for greater clarity) in figure 12. They reveal the complexity of the motion at the surface and some of the processes that clearly influence the loading.

Run-up on the front of the cylinder increases rapidly, with a distinctive thickening at its leading edge, and when the crest is alongside the cylinder (figure 12*a*), depressions at the rear reach down more than one radius below the surrounding water surface. At this stage the incident velocity is at a maximum and the incident acceleration is zero, so the expected water pressures are those that arise through the velocity-squared term of Bernoulli's equation, increasing (as seen in figure 11) to maxima on the upstream and downstream sides of the cylinder, and falling to a minimum abreast of it. Only some of these features can be identified in figure 12(*a*).

At the time corresponding to M_2 (figure 12*b*), there is an upwelling at the centre of the rear face, and the run-up at the front has started to fall back. The dominant feature at the time of M_3 (figure 12*c*) is a mound of water at the rear of the cylinder, and reduced depressions at the sides that start to propagate in the direction opposite to that of wave advance. By the time of M_4 (figure 12*d*), the upwelling at the rear has started to collapse, but the advancing depressions at the sides have coalesced at the front face of the cylinder where a pronounced dip appears.

The presence of strong vertical accelerations makes it difficult to interpret these observations in terms of the pressure recordings, though it seems likely that the lowering of the water surface at the front of the cylinder at the end of the cycle is linked to the reduction in moment at M_4. In the later stages of the process the water surface broke at the rear of the cylinder, as can be seen in figure 12(*c*, *d*). However, though some splashing occurred in all cases, large-scale aeration of the flow was not observed.

https://doi.org/10.1017/S002211209700699X Published online by Cambridge University Press

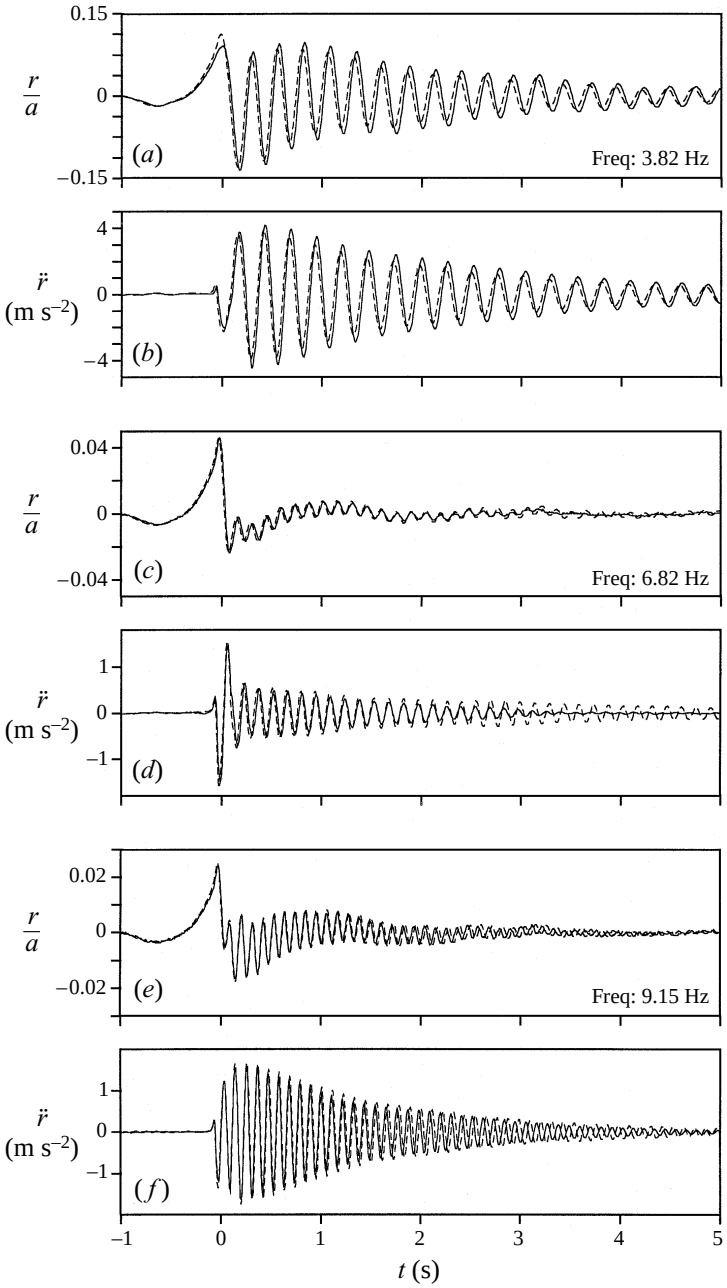


FIGURE 13. Displacement and acceleration records for the 100 mm cylinder in case 775. Continuous lines are measurements, broken lines are computed with the quasi-static model.

3.4. *Ringing response*

In ringing experiments, each cylinder was supported in turn in the 750 mm wide flume as described previously on a system of springs that allowed easy adjustment of stiffness. Natural frequencies ω_c mentioned below are those observed in free oscillations in still water. Some typical ringing responses are shown in figures 13 and 14 in the form of horizontal displacements r and accelerations $\ddot{r}$ at still water level. These are for the

https://doi.org/10.1017/S002211209700699X Published online by Cambridge University Press

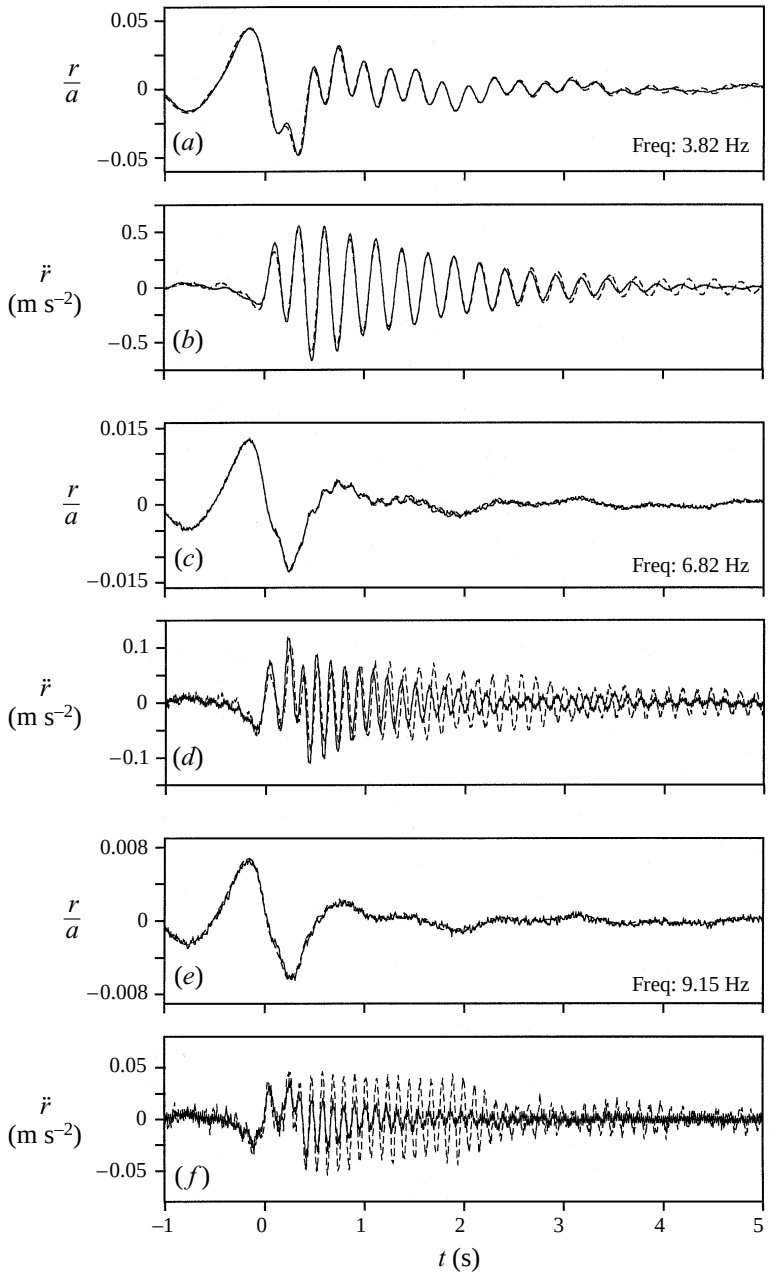


FIGURE 14. Displacement and acceleration records for the 100 mm cylinder in case 745. Continuous lines are measurements, broken lines are computed with the quasi-static model.

100 mm cylinder in cases 775 and 745 respectively, at frequency settings $\omega_c/2\pi = 3.82$, 6.82 and 9.15 Hz (or, in relation to the trough-to-trough period of the waves, at frequency ratios of 4.0, 7.2 and 9.6). In terms of kA the wave in case 775 is about 10% larger than the largest wave observed at the Tern platform over two years (figure 3; Atkins *et al.* 1997). It is therefore very pertinent to design problems for extreme waves in the North Sea. The wave in case 745 is about 40% smaller.

https://doi.org/10.1017/S002211209700699X Published online by Cambridge University Press

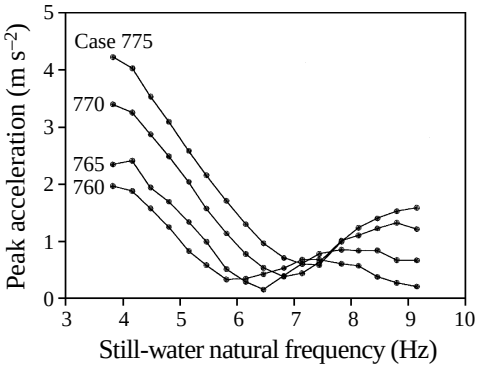


FIGURE 15. The magnitude of the second negative acceleration peak at the still-water level, recorded on the 100 mm diameter cylinder in the four largest waves.

In the low-frequency case, the response records (figures 13 and 14*a*, *b*) follow the behaviour previously observed for example by Jefferys & Rainey (1994), in that the maximum acceleration and the maximum in the high-frequency part of the displacement record occur after the first few half-cycles of the motion. This is the case also at the highest frequency setting (*e*, *f*). But the response at the middle frequency (*c*, *d*) is quite different, since here, particularly in case 775, the acceleration is suddenly reduced by about one-half immediately after the first cycle. This type of motion occurs when the cylinder's natural period is close to the time interval between M_1 and M_2, or in other words when the second peak in the loading opposes the motion of the cylinder that is generated by the first. In figure 15, the magnitude of the second negative acceleration peak is plotted against the cylinder's still-water natural frequency for the 100 mm cylinder in each of the four largest waves. These peak accelerations reach minimum values at still-water natural frequencies between 5.8 Hz (case 760) and 7.2 Hz (775). Owing to the presence of additional added mass during the passage of the crest (see below), the actual initial oscillation frequencies were lower than those measured in still water, and in these cases were close to 4.5 and 6.5 Hz respectively. The corresponding periods (0.22 and 0.16 s) match the intervals between M_1 and M_2 in the same waves, namely 0.23 and 0.16 s.

On this basis it seems reasonable to expect that large amplitudes will occur when the time interval between M_1 and M_2 is close to 50% or 150% of the period of the cylinder's natural frequency oscillations. These conditions would occur in case 760 at frequencies of 2.2 and 6.5 Hz, and in case 775 at 3.1 and 9.4 Hz. Such trends can clearly be detected in figure 15.

In studying the cylinder's ringing response we introduce a reference displacement and a reference acceleration (both at still water water level) based on a model of the cylinder as an undamped elastic system of rotational stiffness K, and constant moment of inertia K/ω_c^2. The reference displacement R is that associated with a statically applied moment of magnitude M_1,

$$R = M_1 l/K, \tag{5}$$

where l is the depth of the pivot below still-water level. A suitable reference acceleration is $R\omega_c^2$, which is the maximum that would occur in the undamped system if the moment M_1 were applied as a step change. Measured peak displacements r_{max} and accelerations $\ddot{r}_{max}$ are related to these scales through factors α and β:

$$r_{max} = \alpha R, \quad \ddot{r}_{max} = \beta R\omega_c^2. \tag{6}$$

https://doi.org/10.1017/S002211209700699X Published online by Cambridge University Press

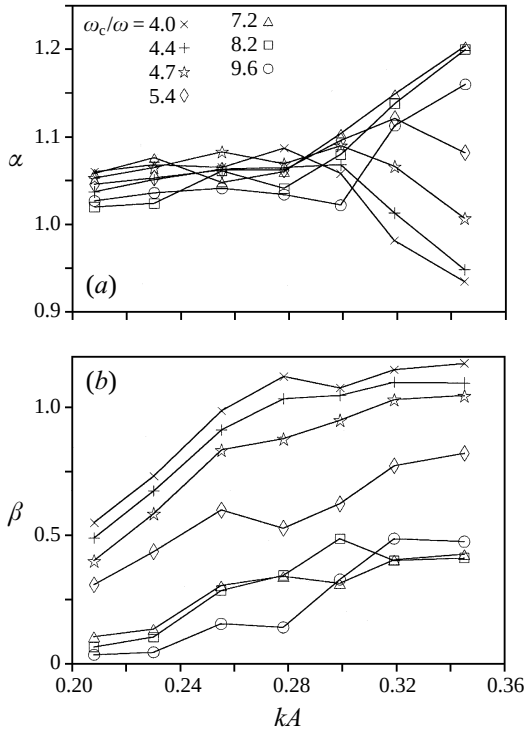


FIGURE 16. Normalized peak displacements (*a*), and accelerations (*b*), for the 100 mm cylinder at various frequency ratios as functions of wave steepness.

In each test r_{max} was identified as the magnitude of the first excursion of the cylinder in the direction of wave. Peak accelerations $\ddot{r}_{max}$ represent half the difference between maximum and minimum measured values.

The factor α is simply the dynamic magnification of the system, referred to the peak loading M_1. And if β were equal to unity, this would imply that the cylinder's maximum acceleration was equal to that which would result (in the absence of damping) if the moment M_1 were applied as a step change. For the 100 mm cylinder, α and β are shown for various frequency ratios ω_c/ω as functions of the wave steepness kA in figure 16. Except in the two steepest waves, α is between 1.0 and 1.1, implying that the peak displacement was not much affected by dynamic magnification. The largest response occurred at the lowest frequency settings in the steepest waves, and here α falls below 1.0, presumably because of increased hydrodynamic damping. Acceleration factors (figure 16*b*) increase roughly with the cube of the wave steepness initially, but they seem to reach limiting values not much greater than 1.0 in the steepest waves.

Three distinct influences on α and β can be identified: the frequency content of the loading, hydrodynamic damping and other interactions between the moving cylinder and the fluid, and the changing immersion of the upper part of the cylinder. The last of these may have an important effect on the motion, because it will lead to rapid changes in added mass as the wave crest passes the cylinder. And in our experiments, changes in added mass were rather important because the motion of the cylinder was always in the form of rotation about the pivot at its base. When the largest wave was alongside the 100 mm cylinder, the added mass associated with that part of the cylinder

https://doi.org/10.1017/S002211209700699X Published online by Cambridge University Press

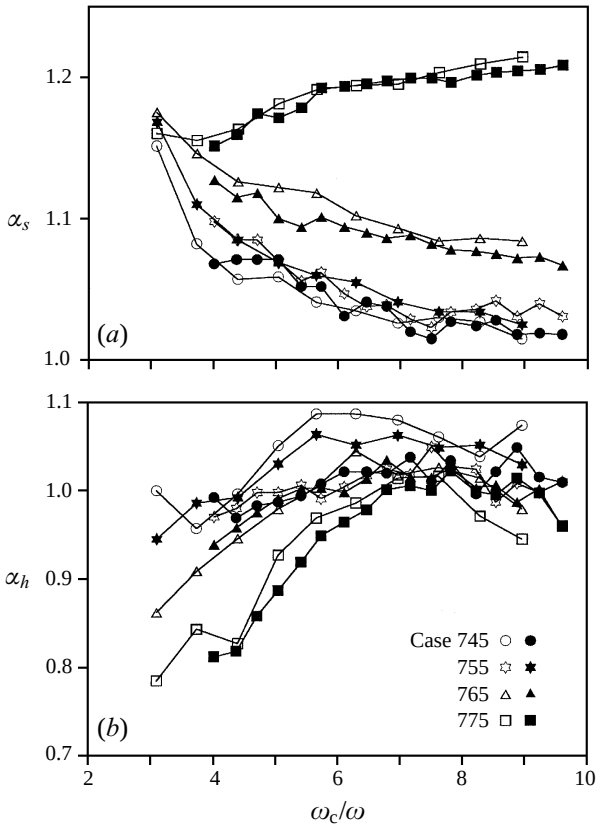


FIGURE 17. Displacement factors α_s and α_h as functions of the ratio of the cylinder's natural frequency to the wave frequency. Closed and open symbols refer to the 100 mm and 127 mm cylinders respectively.

between the still-water level and the undisturbed crest elevation would have been responsible for about 25% of its total moment of inertia. For the 127 mm cylinder the proportion was about 30%. These ratios are unrepresentatively large for offshore structures, but their effect on the response can be predicted as described below.

3.5. *Comparisons with a quasi-static numerical model*

To distinguish between structural and hydrodynamic influences on the response, α and β may be considered in two parts:

$$\alpha = \alpha_s \alpha_h, \quad \beta = \beta_s \beta_h, \tag{7}$$

where α_s and β_s are defined in the same way as α and β in equation (6), but in terms of peak displacements r_{max} and accelerations $\ddot{r}_{max}$ obtained from a time-stepping numerical model rather than from measurements. The model used for this purpose represented the cylinder as an idealized single-degree-of-freedom elastic system, subject to the loading measured in the stiffly supported case. It followed the Newmark integration scheme with linearly varying accelerations over time increments identical to those of the data collection. The motion of the cylinder was computed on the assumptions that the added mass extended up to the undisturbed instantaneous water surface, and that the added mass coefficient and the hydrodynamic damping factor were equal to those observed in free oscillations in still water.

https://doi.org/10.1017/S002211209700699X Published online by Cambridge University Press

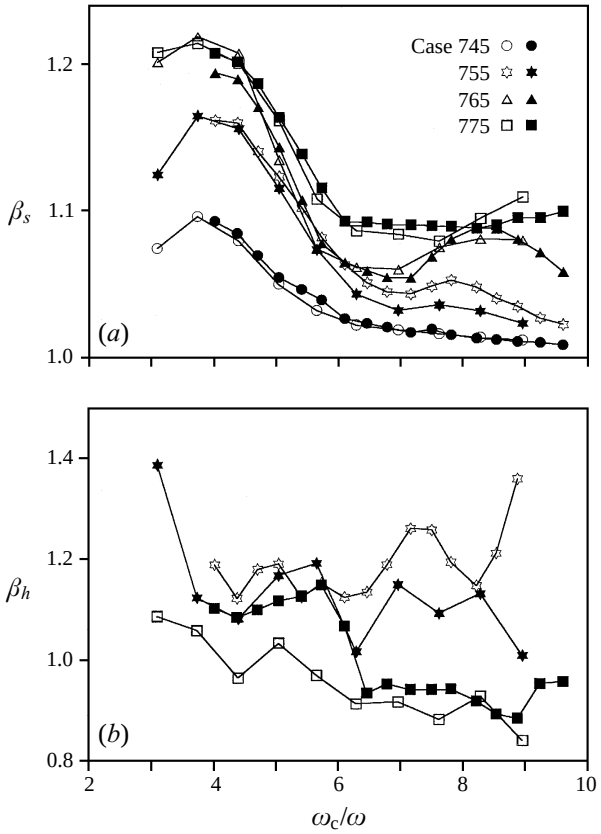


FIGURE 18. Acceleration factors β_s and β_h as functions of the ratio of the cylinder's natural frequency to the wave frequency. Closed and open symbols refer to the 100 mm and 127 mm cylinders respectively.

The factors α_h and β_h, defined as

$$\alpha_h = \frac{\text{measured peak displacement}}{\text{quasi-static peak displacement}}, \quad \beta_h = \frac{\text{measured peak acceleration}}{\text{quasi-static peak acceleration}}, \tag{8}$$

represent the effects of feedback from the cylinder's motion to the loading.

The numerical model used only the measured loads, and therefore neglected all effects of cylinder motion, such as those arising through the Morison drag term and the slender-body corrections to the Morison formulation, represented in figures 6 and 7. Also, additional slender-body terms come into play once the cylinder begins to move. These include the 'negative centrifugal force', the transverse buoyancy, and the position dependence of all the wave loading terms (Rainey 1995*b*).

For each case in figures 13 and 14, the responses computed with the quasi-static model are shown as broken lines. There is generally a good match with measured displacement and acceleration records, suggesting at least that the loading is not profoundly modified by the cylinder's response (a conclusion reached also by Jefferys & Rainey 1994), and that responses for a cylinder of different dynamic properties could equally well be predicted from the same loading record. But, as in Jefferys & Rainey's case, there are some important differences between measured and simulated responses, suggesting in other words that α_h and β_h may not always be close to unity.

https://doi.org/10.1017/S002211209700699X Published online by Cambridge University Press

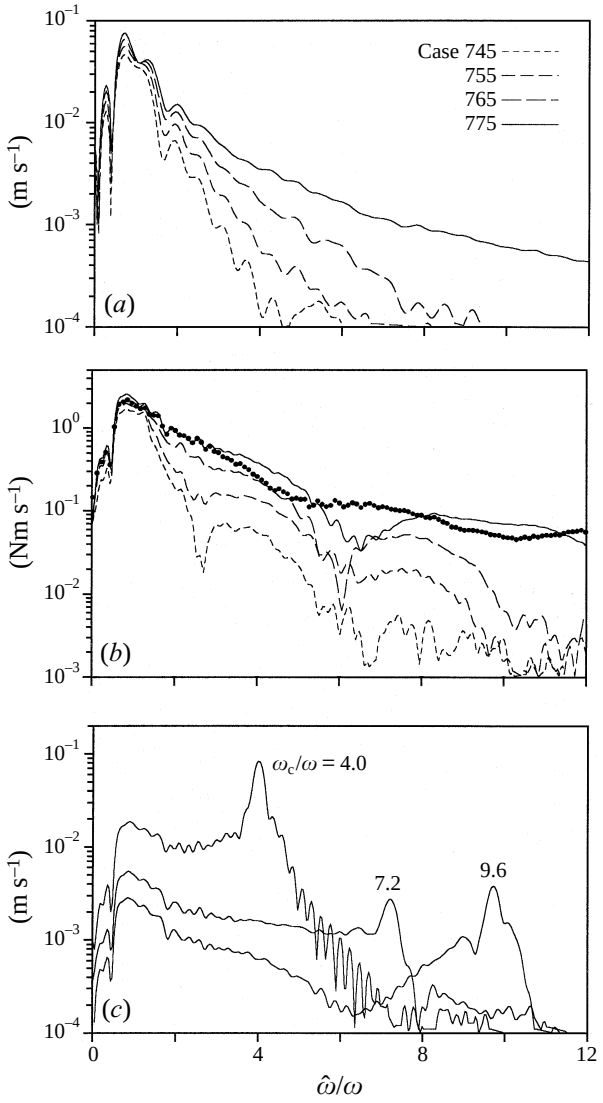


FIGURE 19. Moduli of Fourier transforms of (*a*) water surface elevation records, (*b*) the moment measured on the 100 mm cylinder in the stiffly supported condition, and (*c*) the response of the 100 mm cylinder at the three frequency settings in case 775 whose time series are plotted in figure 13.

Quasi-static dynamic magnification factors α_s are plotted in figure 17(*a*) as functions of the frequency ratio ω_c/ω for four wave amplitudes. Dynamic effects in the displacement response are important where α_s departs significantly from unity, i.e. at the lowest frequency ratios in all waves, and at all frequency ratios in the largest waves, where α_s approached 1.2. Other hydrodynamic factors clearly also influence the peak displacements in some cases, as shown in figure 17(*b*) by the departure of α_h from unity. For most tests α_h was between 0.9 and 1.1, but it was less than 0.9 for low frequency ratios in large waves. These are the cases where the cylinder's velocity was highest, and therefore where the relative motion terms above, absent in the computations, would be most important.

https://doi.org/10.1017/S002211209700699X Published online by Cambridge University Press

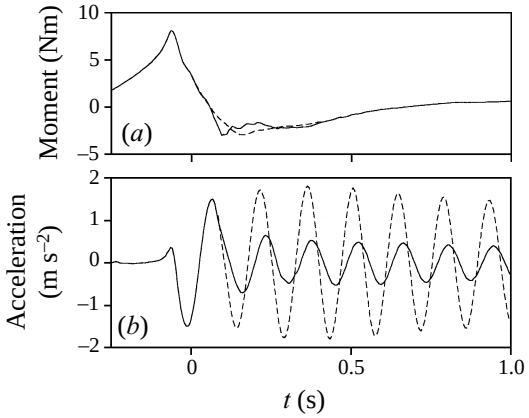


FIGURE 20. The effect of the secondary loading cycle on the response. Computed responses are shown in (*b*) for the moments in (*a*) at a frequency ratio of 7.2. Case 775.

The acceleration factor β_s (figure 18*a*) revealed much stronger frequency-dependent behaviour. In the largest waves, at almost the lowest frequency ratios, β_s reached maximum values slightly above unity, indicating that computed accelerations were greater than those which would occur if the maximum moment M_1 were applied as a step change to the idealized system with no damping. Measured peak accelerations were still larger by an average of about 10%, as shown in figure 18(*b*) where the ratio between measured and predicted peak accelerations β_h is plotted for two cases. The results are scattered between 0.9 and 1.3 without obvious trends.

In the middle range of wave heights there is a minimum in the peak acceleration factor β_s where the period of the cylinder's oscillations was close to the time interval from M_1 to M_2, as discussed above. This is apparent also in the frequency domain. Since the water surface elevation record and the loading and response of the cylinder are all transients, it is appropriate to examine their spectral content by computing their true, rather than their finite, Fourier transforms, and this was achieved by numerical integration over the interval $-1 < t < 5$ s, after the signals had been tapered smoothly to zero over 0.5 s at each end. Moduli of Fourier transforms computed in this way are plotted in figure 19 against the ratio of frequency $\hat{\omega}$ to wave frequency ω. In the range $6 < \hat{\omega}/\omega < 7$, the Fourier transforms of moment on the stiffly supported cylinder (figure 19*b*) have minima that are not present in the wave itself (figure 19*a*), but are evidently related to those in β_s (figure 18*a*) and in peak accelerations (figure 15) in the same frequency range. Figure 19(*c*) shows a correspondingly weaker response at $\omega_c/\omega = 7.2$ than at $\omega_c/\omega = 4.0$ or 9.6.

The sensitivity of the cylinder's response to the secondary loading cycle is demonstrated in figure 20, where two computed acceleration records are compared for the 100 mm cylinder at a frequency ratio of 7.2 in case 775. First, the measured moment (whose Fourier transform is shown in figure 19*b*), and the response computed from it (in close agreement with the measured response shown in figure 13*d*), are shown as continuous lines. Since this case is in the intermediate frequency range, there is a substantial reduction of the motion after the first cycle, as noted above. Secondly, broken lines show the effect of an artificial modification made to smooth out the secondary loading cycle from the moment record. The resulting Fourier transform is shown as a series of points in figure 19(*b*), differing from the original by the absence of a minimum at frequency ratios between 6 and 7. Correspondingly, the response

https://doi.org/10.1017/S002211209700699X Published online by Cambridge University Press

computed from the modified moment record (shown as a broken line in figure 20*b*) does not undergo a rapid attenuation, and large-amplitude oscillations are sustained.

These differences (which were found over a wide range of frequency ratios) are the consequences of rather arbitrary changes to the loading record, but they illustrate the problem of obtaining accurate predictions of response from models that are unable to capture the complex fluid motion around the cylinder at the free surface.

4. Conclusions

Measurements of ringing were obtained in laboratory experiments on single bottom-pivoted vertical cylinders in focused waves, over frequency ratios (cylinder natural frequency to wave frequency) between 3 and 11. Within an intermediate range of frequencies the motion exhibited a sudden reduction after the first cycle, caused by a coincidence of the cylinder's natural period with the time interval between positive and negative peaks in the loading. At other natural frequencies the same reversal in the loading led to an enhancement of the response.

Peak forces and moments measured on the same cylinders when stiffly supported in the same waves exceeded Morison predictions (based on the kinematics of an unsteady model of the measured waves) by a margin that increased rapidly with wave steepness. Much better agreement was achieved when slender-body corrections to Morison's equation, which improve the accuracy of its inertia term in modelling potential flow loads, were included. Similar force computations based on regular wave kinematics (using the measured wave height and period) led to significant under-prediction of the peak loading.

The acceleration response of flexibly mounted cylinders at low frequency ratios was limited approximately to that which would occur if the peak static loading were applied, in the absence of damping, as a step change. Maximum accelerations were observed at frequency ratios of about 3.5. Accelerations at higher frequencies were not dissimilar to those that would arise from a resonant response at the level of damping observed in still water.

In most cases measurements of response were found to agree closely with those computed by a time-stepping numerical model based on statically measured forces. However, hydrodynamic factors (feedback from the motion to the loading) were clearly important in the largest waves and lowest frequency ratios, producing at most a 20% reduction in peak displacements. Peak accelerations (much more sensitive to the frequency ratio) were scattered between about 90% and 125% of the quasi-static predictions.

Tank wall effects were surprisingly unimportant. Force records obtained at blockage ratios (cylinder diameter to tank width) of 0.13 and 0.25 were found to be almost indistinguishable, except for an enhancement of the peak loading in the steepest waves by about 8%. In waves of about 72% of limiting height, the difference was less than 2.5%.

Particular attention was given to a secondary loading cycle (previously described by Grue *et al.* 1993) that occurs after the crest has passed the cylinder's axis. The amplitude of this oscillation was found to be a function predominantly of the wave steepness, and simple numerical experiments showed that it may have an important effect on ringing response.

This work was supported by the EPSRC, through grant number GR/J53317.

https://doi.org/10.1017/S002211209700699X Published online by Cambridge University Press

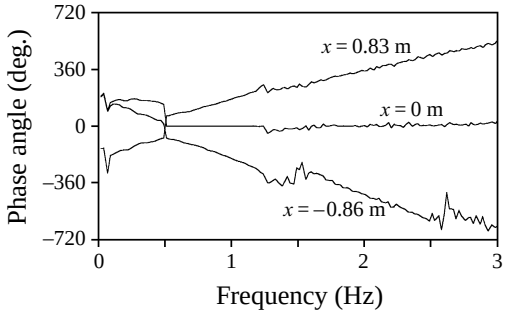


FIGURE 21. Phase angles close to the focus point. The wave conditions were close to those of case 775.

Appendix. Generating focused waves

Generating large individual waves in water of uniform depth by frequency focusing can be achieved by at least three different approaches. Those that are referred to most often in the literature are: first, arranging for mutual reinforcement at a particular point in the tank between many component wave trains of different frequencies (Greenhow *et al.* 1982); secondly, using a waveboard control signal derived from the computed dispersion of waves following the release of a given volume of water placed on an initially still water surface (Mansard & Funke 1982); and third, generating waves of continuously changing frequency into still water in such a way that the energy at all frequencies arrives simultaneously at the focal point (Longuet-Higgins 1974).

The generation of the waveboard control signal in each case may be worked out with linear theory, and for many purposes this provides an adequate approximation. But it is found that because of nonlinearities the wave components do not come to a true focus, and that changes in the amplitude of the waveboard's motion produce unpredictable changes in the waves. It was desirable to conduct the present experiments in large waves of various amplitudes, and for this purpose we used the first approach described above, but rather than relying on linear theory we developed an empirical technique for ensuring accurate phase convergence of all the component waves at the target focal point in each case.

The frequencies of the mechanically generated waves corresponded to those 34 sub-multiples of an overall repeat period of 45 s that were within the range 0.8 to 2 s. They were therefore equally spaced between 0.511 and 1.244 Hz, covering most of the useable bandwidth of the waveboard. In each case, their amplitudes were set approximately mid-way between the conditions of uniform amplitude and of uniform steepness. An initial estimate of the waveboard control signal was generated after computing the required phase of each component from linear theory.

In the absence of the cylinder, but with a wave gauge at its mounting position (the focal point), the control signal was played out repeatedly to the waveboard while the output of the wave gauge was digitized at a rate corresponding to 8192 samples in the overall repeat period, i.e. at a frequency of 182.04 Hz. The phase of each mechanically generated wave component at the wave gauge was then computed by fast Fourier transform (FFT). For the next iteration, an exactly opposite phase shift was applied to the corresponding component of the waveboard's control signal, and the whole process was repeated until convergence. This operation was carried out for each of the seven cases listed in table 1, and was found to be very stable. It was rarely necessary to complete more than three iterations before all mechanically generated wave components were in phase at the focal point to well within one degree, producing a

https://doi.org/10.1017/S002211209700699X Published online by Cambridge University Press

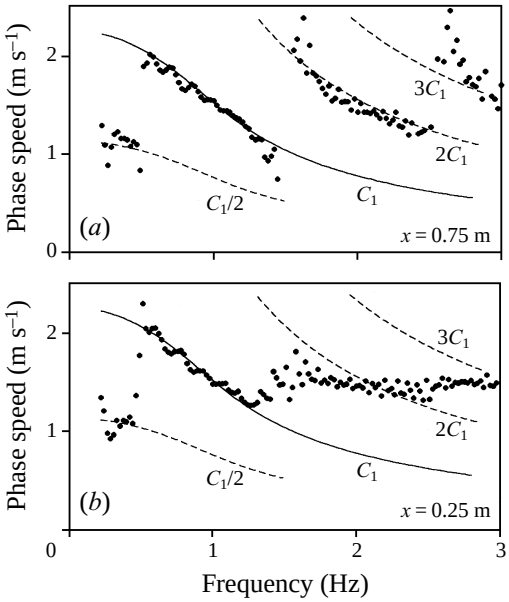


FIGURE 22. Phase speeds measured at points close to the focus; C_1 denotes the linear phase speed.

focused wave there exactly at the end of each repeat period. The same technique has been used to generate breaking and non-breaking focused waves, in several different wave flumes, both in the absence of structures (over a wide range of focal distances), and against a vertical wall.

Phases of the wave components measured around the focal point in the present experiments, in conditions close to those of case 775 of table 1, are shown in figure 21, where x is measured from the focal point in the direction of wave advance. Over the frequency range corresponding to the mechanically generated waves, the wave components at $x = 0$ m are very nearly at a common phase of zero (corresponding to a maximum horizontal velocity), as intended. The naturally generated waves at higher frequencies are also close to zero phase at this point, though they have undergone a phase shift between $x = -0.86$ and 0 m. Those at lower frequencies below the range of mechanically generated waves are predominantly at a phase of 180° at $x = 0$ m, in accordance with the expected behaviour of the long wave that travels with the group.

Phase speeds of the same waves were computed as a function of frequency from the FFT of water surface elevation records obtained at adjacent pairs of wave gauges, and are shown in figure 22 at two locations ahead of the focal point. At $x = -0.75$ m, low-frequency waves appear at about one-half of the linear phase speed, while at frequencies greater than those of the mechanically generated waves, phase speeds are close to two and three times the linear result, in agreement with the case of the single modulated wavetrain discussed by Crawford *et al.* (1981).

But at $x = -0.25$ m the high-frequency waves have an almost uniform phase speed, close to that corresponding to the middle of the range of mechanically generated waves. This behaviour (similar to that in cases with continuous spectra studied by Crawford *et al.*) continued for about 1.25 m beyond the focal point (a total distance of more than $2\pi/k$ – from table 1), beyond which the pattern shown in figure 2(*a*) was re-established.

These measurements showed that at the focal point (where the ringing experiments

https://doi.org/10.1017/S002211209700699X Published online by Cambridge University Press

were carried out), wave components over a wide range of frequencies were at a common phase, and that the wave group as a whole propagated with a coherence much greater than that which would be expected from a linear model. Further details of these experiments are described by Chaplin (1996).

REFERENCES

Atkins, N., Lyons, R. A. & Rainey, R. C. T. 1997 Summary of findings of wave load measurements on the Tern platform. *HSE Rep*. OTH 95 467. HSE Books, London.

Baldock, T. E. & Swan, C. 1994 Numerical calculations of large transient water waves. *Appl. Ocean Res*. **16**, 101–112.

Baldock, T. E., Swan, C. & Taylor, P. H. 1995 A laboratory study of nonlinear surface-waves on water. *Phil. Trans. R. Soc. Lond.* A **354**, 649–676.

Chaplin, J. R. 1980 Developments of stream function wave theory. *Coastal Engng* **3**, 179–205.

Chaplin, J. R. 1996 On frequency-focusing unidirectional waves. *Intl J Offshore Polar Engng* **6**, 131–137.

Cokelet, E. D. 1977 Steep gravity waves in water of arbitrary uniform depth. *Phil. Trans. R. Soc. Lond.* A **286**, 183–230.

Crawford, D. R., Lake, B. M., Saffman, P. G. & Yuen, H. C. 1981 Effects of nonlinearity and spectral bandwidth on the dispersion relation and component phase speeds of surface gravity waves. *J. Fluid Mech*. **112**, 1–32.

Dommermuth, D. G., Yue, D. K. P., Lin, W. M., Rapp, R. J., Chan, E. S. & Melville, W. K. 1988 Deep-water plunging breakers – a comparison between potential-theory and experiments. *J. Fluid Mech*. **189**, 423–442.

Faltinsen, O. M., Newman, J. N. & Vinje, T. 1995 Nonlinear wave loads on a slender vertical cylinder. *J. Fluid Mech*. **289**, 179–198.

Greenhow, M., Vinje, T., Brevig, P. & Taylor, J. 1982 A theoretical and experimental study of capsize of Salter's duck in extreme waves. *J. Fluid Mech*. **118**, 221–239.

Grue, J., Bjørshol, G. & Strand, Ø. 1993 Higher harmonic wave exciting forces on a vertical cylinder. *Institute of Mathematics*, *University of Oslo Preprint*, No. 2. ISBN 82-553-0862-8, 28pp.

Jefferys, E. R. & Rainey, R. C. T. 1994 Slender body models of TLP and GBS ringing. *Proc. 7th Intl Conf. on the Behaviour of Offshore Structures*, *BOSS'94*, *Cambridge*, *USA*.

Lake, B. M. & Yuen, H. C. 1978 A new model for nonlinear wind waves. Part 1. Physical model and experimental evidence. *J. Fluid Mech*. **88**, 33–62.

Longuet-Higgins, M. S. 1974 Breaking waves in deep or shallow water. *Proc. 10th Conf. on Naval Hydrodynamics*, pp. 597–605, MIT.

Malenica, S. & Molin, B. 1995 Third-harmonic wave diffraction by a vertical cylinder. *J. Fluid Mech*. **302**, 203–229.

Mansard, E. P. D. & Funke, E. R. 1982 A new approach to transient wave generation. *Proc. 18th Intl Conf. on Coastal Engineering*, pp. 710–724. ASCE.

Natvig, B. J. & Teigen, P. 1993 Review of hydrodynamic challenges in TLP design. *Intl J. Offshore and Polar Engng* **3**, 241–249.

New, A. L., McIver, P. & Peregrine, D. H. 1985 Computations of overturning waves. *J. Fluid Mech*. **150**, 233–251.

Rainey, R. C. T. 1989 A new equation for calculating wave loads on offshore structures. *J. Fluid Mech*. **204**, 295–324.

Rainey, R. C. T. 1995*a* The hydrodynamic load at the intersection of a cylinder with the water surface. *Proc. 10th Intl Workshop on Water Waves and Floating Bodies*, *Oxford University: Dept. Engng Sci.* (ed. R. Eatock Taylor), pp. 207–211.

Rainey, R. C. T. 1995*b* Slender-body expressions for the wave load on offshore structures. *Proc. R. Soc. Lond.* A **450**, 391–416.

Rainey, R. C. T. 1997 Violent surface motion around vertical cylinders in large, steep waves – is it the result of the step change in relative acceleration? *Proc. 12th Intl Workshop on Water Waves and Floating Bodies*, *Marseilles: Ecole Superieure d'Ingenieurs de Marseille* (ed. B. Molin), pp. 215–220.

https://doi.org/10.1017/S002211209700699X Published online by Cambridge University Press

Schwartz, L. W. 1974 Computer extension and analytic continuation of Stokes' expansion for gravity waves. *J. Fluid Mech.* **62**, 553–578.

Stansberg, C. T., Huse, E., Krokstad, J. R. & Lehn, E. 1995 Experimental study of non-linear loads on vertical cylinders in steep random waves. *Proc. 5th Intl Offshore and Polar Engng Conf.*, vol. 1, pp. 75–82.

Zhao, R., Faltinsen, O., Krokstad, J. R. & Aanesland, V. 1988 Wave-current interaction effects on large-volume structures. *Proc. Intl Conf. on the Behaviour of Offshore Structures*, *BOSS'88*, *Trondheim*, *Norway*, vol. 2, pp. 623–638.

https://doi.org/10.1017/S002211209700699X Published online by Cambridge University Press